# Monte Carlo study of two-step defect melting

W. Janke and H. Kleinert
*Institut für Theorie der Elementarteilchen, Freie Universität Berlin, Arnimallee 14, 1000 Berlin 33, Germany*
(Received 31 August 1989)

We present a detailed Monte Carlo study of the recently proposed model of defect melting in two dimensions exhibiting a crossover from a single first-order melting transition to two successive transitions of the Kosterlitz-Thouless type. The distinguishing parameter of this model is the length scale $l$ of rotational stiffness.

## I. INTRODUCTION

In 1979, Halperin, Nelson, and Young[1] (HNY) generalized the Kosterlitz-Thouless[2] (KT) work on superfluid films and suggested that melting in two dimensions should proceed via two successive pair-unbinding transitions. In the first transition, pairs of dislocations should dissociate, while in the second, dislocations are supposed to split into pairs of disclinations. The considerations were phenomenological in character and did not permit specifying the precise physical conditions under which these processes would happen. In fact, when trying to construct definite models that allow for lattice distortions and defects as in the HNY theory, these models have always shown a single first-order melting transition.[3–7] Experimentalists, on the other hand, have indeed seen two-step melting, although not in atomic lattices[8] but only in layers of molecular crystals.[9] These consist of rodlike molecules to which the original HNY theory does not really apply. In these layers, the number of degrees of freedom is larger than in an atomic crystal and cannot be described satisfactorily by a single displacement field with classical elastic energy.

Recently, it has been pointed out[10] that the experimental situation can be accounted for by the introduction of an additional elastic term, accounting for the rotational stiffness of the system,

$$E_{\rm el}^{(2)}=2\mu l^2\int d^2x\,(\partial_i\omega)^2\ , \tag{1}$$

where

$$\omega(\mathbf{x})=\tfrac{1}{2}[\partial_1 u_2(\mathbf{x})-\partial_2 u_1(\mathbf{x})] \tag{2}$$

is the local rotation angle of the displacement field $u_i(\mathbf{x})$. This term is observable in the transverse frequency spectrum as the coefficient of order $k^4$ (Ref. 11),

$$\omega_T^2=c^2k^2(1+l^2k^2+\cdots)\ .$$

In a general anisotropic crystal, the coefficient $l^2$ depends on the direction of the momentum vector. For simplicity, we shall assume the anisotropy to be sufficiently small to allow ignoring this dependence.

Together with the ordinary elastic energy

$$E_{\rm el}^{(1)}=\int d^2x\left[\mu u_{ij}^2+\frac{\lambda}{2}u_{ii}^2\right]\ , \tag{3}$$

the model is then constructed on the basis of the combined second-gradient elastic energy

$$E_{\rm el}=E_{\rm el}^{(1)}+E_{\rm el}^{(2)}\ . \tag{4}$$

As usual, $u_{ij}(\mathbf{x})$ is the strain tensor

$$u_{ij}(\mathbf{x})=\tfrac{1}{2}[\partial_i u_j(\mathbf{x})+\partial_j u_i(\mathbf{x})]\ . \tag{5}$$

The energy $E_{\rm el}$ is extended by plastic distortions and rotations, replacing $\partial_i u_j$, $u_{ij}$, and $\partial_i\omega$ by[10,12,13]

$$\begin{aligned}&\partial_i u_j^{\rm el}=\partial_i u_j-\beta_{ij}^P\ ,\\ &u_{ij}^{\rm el}=u_{ij}-u_{ij}^P,\quad u_{ij}^P=\tfrac{1}{2}(\beta_{ij}^P+\beta_{ji}^P)\ ,\\ &\partial_i\omega^{\rm el}=\partial_i\omega-\tfrac{1}{2}\partial_i\epsilon_{jk}\beta_{jk}^P-\kappa_i^P\ .\end{aligned} \tag{6}$$

Finally, the system is formulated on a lattice with spacing $a$, replacing derivatives by $a^{-1}$ times the lattice differences

$$\nabla_i f(\mathbf{x})=f(\mathbf{x}+\mathbf{i})-f(\mathbf{x})\ , \tag{7}$$

where $\mathbf{i}$ are the link vectors to the nearest neighbors. For simplicity, the lattice was at first taken to be of the square type. On the lattice, the plastic distortions are quantized, being integer multiples of the lattice spacing $a$. Without the $l^2$ term, the model has been studied in great detail.[3–6] It undergoes a first-order melting transition in which chains of dislocation-antidislocation pairs proliferate. This is similar to the grain-boundary mechanism proposed by Chui.[14] As we shall now see, the $l^2$ term allows to split these transitions into two steps, each of them being of the Kosterlitz-Thouless type.

## II. THE MODEL

As explained in the Introduction the combined energy, $E_{\rm el}\equiv E_{\rm el}^{(1)}+E_{\rm el}^{(2)}$, is placed on a square lattice of spacing $a$, with the gradients $\partial_i$ replaced by $(1/a)\nabla_i$. Fur-

 

thermore, we shall rescale the displacements $u_i \in (-a/2, a/2)$ to $\gamma_i = 2\pi u_i/a \in (-\pi, \pi)$ and $\omega$ to $\frac{1}{2}\epsilon_{ij}\nabla_i\gamma_j$. We can then replace the plastic distortions $\beta_{ij}^P$ and $\kappa_i^P$ by the integer-values plastic quantities $n_{ij}$ and $m_i$. These supply the Volterra jumping surfaces, whose boundaries are dislocations and disclinations. Setting $\beta \equiv a^2\mu/(2\pi)^2 k_B T$, the ensuing model partition function has the "distortion-plus-defect" form[10,13]

$$Z_1 = \prod_{\mathbf{x}} \left[ \int_{-\pi}^{\pi} d^2\gamma \right] \sum_{\substack{\{n_{ij}\} \\ \{m_i\}}} \exp\left\{ -\beta \left[ \frac{1}{4} \sum_{\mathbf{x},i,j} (\nabla_i\gamma_j + \nabla_j\gamma_i - 4\pi n_{ij}^s)^2 + \frac{\lambda}{2\mu} \sum_{\mathbf{x}} \left[ \sum_i [\nabla_i\gamma_i(\mathbf{x}-\mathbf{i}) - 2\pi n_{ii}^s(\mathbf{x}-\mathbf{i})] \right]^2 \right.\right.$$
$$\left.\left. + \frac{2l^2}{a^2} \sum_{\mathbf{x},i} [\nabla_i\omega - 2\pi(m_i + \nabla_i n_{12}^a)]^2 \right] \right\}, \tag{8}$$

where we have introduced $n_{ij}^s \equiv (n_{ij} + n_{ji})/2$ and $n_{12}^a \equiv (n_{12} - n_{21})/2$.[10] For $l = 0$, this partition function is easily seen to reduce to the "strain-plus-defect" melting model studied previously[3-7] (up to an overall infinite constant)

$$Z_1^{l=0} = \prod_{\mathbf{x}} \left[ \int_{-\pi}^{\pi} d^2\gamma \right] \sum_{\substack{\{N_{ij}\} \\ i \le j}} \exp\left\{ -\beta \left[ \frac{1}{2} \sum_{\mathbf{x}} (\nabla_1\gamma_2 + \nabla_2\gamma_1 - 2\pi N_{12})^2 + \xi \sum_{\mathbf{x},i} (\nabla_i\gamma_i - 2\pi N_{ii})^2 \right.\right.$$
$$\left.\left. + \frac{\lambda}{2\mu} \sum_{\mathbf{x}} \left[ \sum_i [\nabla_i\gamma_i(\mathbf{x}-\mathbf{i}) - 2\pi N_{ii}(\mathbf{x}-\mathbf{i})] \right]^2 \right] \right\}, \tag{9}$$

with integers $N_{12} = n_{12} + n_{21}$, $N_{ii} = n_{ii}$, and the anisotropy parameter $\xi \equiv (c_{11} - c_{12})/2c_{44}$ taken to be 1 (isotropic case).

## III. ALTERNATIVE REPRESENTATIONS

For the theoretical as well as the numerical analysis of the model (8), it is more convenient to use one of the following equivalent representations. By a quadratic completion one obtains, apart from a trivial overall factor,[7]

$$Z_2 = \prod_{\mathbf{x}} \left[ \int d^2\gamma \int d\omega \int d\sigma_{ij} \int d\tau_i \right]$$
$$\times \sum_{\substack{\{n_{ij}\} \\ \{m_i\}}} \Phi[n_{ij}, m_i] \exp\left\{ -\frac{1}{\beta} \sum_{\mathbf{x}} \left[ \frac{1}{4} \left[ \sigma_{ij}^{s2} - \frac{\nu}{1+\nu} \sigma_{ii}^{s2} \right] + \frac{1}{8l^2/a^2} \tau_i^2 \right] \right.$$
$$\left. + i \sum_{\mathbf{x}} [\sigma_{ij}(\nabla_i\gamma_j - 2\pi n_{ij} - \epsilon_{ij}\omega) + \tau_i(\nabla_i\omega - 2\pi m_i)] \right\}. \tag{10}$$

The auxilliary variables $\sigma_{ij}$ and $\tau_i$ are the stresses and torque stresses of the system, respectively, and $\sigma_{ij}^s \equiv \frac{1}{2}(\sigma_{ij} + \sigma_{ji})$. Summations over $i, j = 1, 2$ are implied, and $\sigma_{ii}^{s2}$ stands short for

$$\sigma_{ii}^{s2} \equiv \left[ \sum_i \sigma_{ii}^s(\mathbf{x}-\mathbf{i}) \right]^2 .$$

The parameter $\nu = \lambda/(\lambda + 2\mu)$ ($= \lambda/[(D-1)\lambda + 2\mu]$ in $D$ dimensions) is Poisson's ratio. The functional $\Phi[n_{ij}, m_i]$ is a gauge fixing factor needed to remove the degeneracy with respect to the integer-valued local-defect gauge transformations[3,4,7,12]

$$\begin{aligned} &\omega \to \omega + 2\pi M, \quad m_i \to m_i + \nabla_i M , \\ &\gamma_i \to \gamma_i + 2\pi N_i, \quad n_{ij} \to n_{ij} + \nabla_j N_i - \epsilon_{ij} M . \end{aligned} \tag{11}$$

Integrating out $\gamma_i$ and $\omega$ leads to the stress conservation laws [with the dual lattice difference $\overline{\nabla}_i f(\mathbf{x}) \equiv f(\mathbf{x}) - f(\mathbf{x}-\mathbf{i})$]

$$\begin{aligned} &\overline{\nabla}_i \sigma_{ij} = 0 \\ &\overline{\nabla}_i \tau_i = \epsilon_{ij}\sigma_{ij} . \end{aligned} \tag{12}$$

These are automatically satisfied by introducing the stress gauge fields $A_i$ and $h$ via

$$\sigma_{ij}=\epsilon_{ik}\overline{\nabla}_k A_j \ , \qquad \tau_i=\epsilon_{ij}\overline{\nabla}_j h + A_i \ . \tag{13}$$

In terms of these fields the partition function becomes[7,10,12,13]

$$Z_3=\sum_{\begin{Bmatrix} n_{ij} \\ m_i \end{Bmatrix}} \Phi[n_{ij},m_i]\int_{-\infty}^{\infty} dA_i \int_{-\infty}^{\infty} dh \exp\left\{-\frac{1}{\beta}\sum_{\mathbf{x}}\left[\frac{1}{4}\left[\frac{1}{1+\nu}(\overline{\nabla}_i A_j)^2-\frac{1}{2}\frac{1-\nu}{1+\nu}(\overline{\nabla}_i A_i)^2\right]\right.\right.$$
$$\left.\left.+\frac{1}{8l^2/a^2}(\overline{\nabla}_i h-\epsilon_{ij}A_j)^2\right]-2\pi i\sum_{\mathbf{x}}(A_i b_i+h\Theta)\right\}, \tag{14}$$

where

$$b_i\equiv\epsilon_{jk}\nabla_j n_{ki}+m_i \ , \qquad \Theta\equiv\epsilon_{ij}\nabla_i m_j \ . \tag{15}$$

are the integer-valued dislocation and disclination densities. They are invariant under the defect gauge transformations (11), and sums over the defect gauge fields with gauge fixing are equal to the sum over the defect densities,

$$\sum_{\begin{Bmatrix} n_{ij} \\ m_i \end{Bmatrix}} \Phi[n_{ij},m_i]=\sum_{\begin{Bmatrix} b_i \\ \Theta \end{Bmatrix}} \ . \tag{16}$$

Doing the summations over the defect densities, the stress gauge fields are squeezed onto integers, yielding the roughening representation

$$Z_4=\sum_{\{A_i,h\}}\exp\left\{-\frac{1}{\beta}\sum_{\mathbf{x}}\left[\frac{1}{4}\left[\frac{1}{1+\nu}(\overline{\nabla}_i A_j)^2-\frac{1}{2}\frac{1-\nu}{1+\nu}(\overline{\nabla}_i A_i)^2\right]+\frac{1}{8l^2/a^2}(\overline{\nabla}_i h-\epsilon_{ij}A_j)^2\right]\right\}. \tag{17}$$

This form was found most useful for our numerical work.[13]

For $l=0$, the last term enforces

$$A_i=\epsilon_{ij}\overline{\nabla}_j h \ , \tag{18}$$

and $Z_4$ reduces to the Laplacian roughening (LR) model[15]

$$Z_4^{l=0}\equiv Z_{\mathrm{LR}}=\sum_{\{h\}}\exp\left[-\frac{\beta_{\mathrm{LR}}}{2}\sum_{\mathbf{x}}(\overline{\nabla}\cdot\nabla h)^2\right] \tag{19}$$

with

$$\beta_{\mathrm{LR}}=\frac{1}{2\beta(1+\nu)} \ . \tag{20}$$

This is, of course, the well-known dual representation of the "strain-plus-defect" partition function $Z_1^{l=0}$ [of Eq. (9)] for $\xi=1$. Notice that the $\lambda$ term in (9) enters only through a multiplicative renormalization $\beta\to\beta(1+\nu)=\beta[1+\lambda/(\lambda+2\mu)]$. This is why we have put $\lambda=0$ in our previous Monte Carlo simulation of $Z_1^{l=0}$.[4,7]

Yet another representation of the model (8) is obtained by integrating out the stress gauge fields in (14), leading to the pure defect representation

$$Z_5=\sum_{\begin{Bmatrix} b_i \\ \Theta \end{Bmatrix}}\exp\left[-4\pi^2\beta(1+\nu)\sum_{\mathbf{x}}\eta\frac{1}{(\overline{\nabla}\cdot\nabla)^2}\eta\right]$$
$$\times\exp\left[-4\pi^2\beta(2l^2/a^2)\sum_{\mathbf{x}}\left[\Theta\frac{1}{-\overline{\nabla}\cdot\nabla}\Theta+\overline{\nabla}_i b_i\frac{1}{-\overline{\nabla}\cdot\nabla[1+(l^2/a^2)(-\overline{\nabla}\cdot\nabla)]}\overline{\nabla}_j b_j\right]\right], \tag{21}$$

with the total defect density

$$\eta\equiv\Theta+\epsilon_{ij}\nabla_i b_j \ . \tag{22}$$

For $l=0$, Eq. (21) reduces to

$$Z_5^{l=0}=\sum_{\{\eta\}}\exp\left[-4\pi^2\beta(1+\nu)\sum_{\mathbf{x}}\eta\frac{1}{(\bar{\nabla}\cdot\nabla)^2}\eta\right], \tag{23}$$

which is, of course, the defect representation of the "strain-plus-defect" partition function $Z_1^{l=0}$ or, equivalently, the dual of the Laplacian roughening model, $Z_4^{l=0}\equiv Z_{\mathrm{LR}}$ [see Eqs. (9) and (19)].

The inverse lattice Laplacians in (21) and (23) describe long-range potentials between defects. In accordance with universality, only their asymptotic behavior is relevant for phase transitions. In order to study these, it is useful to rewrite the defect energy in (21) in a more explicit way

$$\beta E_{\mathrm{def}}=4\pi^2\beta(1+\nu)\sum_{\mathbf{x},\mathbf{x}'}[\Theta(\mathbf{x})v^h(\mathbf{x}-\mathbf{x}')\Theta(\mathbf{x}')+b_i(\mathbf{x})v_{ij}^A(\mathbf{x}-\mathbf{x}')b_j(\mathbf{x}')]+f(\Theta,b_i)+\varepsilon_{\mathrm{core}}, \tag{24}$$

where $f(\Theta,b_i)$ represents $\Theta$ and $b_i$ terms and $\varepsilon_{\mathrm{core}}$ are core energies. Formally, the potential between disclinations is given by

$$v^h(\mathbf{x})\equiv\frac{1}{(\bar{\nabla}\cdot\nabla)^2}(\mathbf{x},0)+\frac{2l^2/a^2}{1+\nu}\frac{1}{(-\bar{\nabla}\cdot\nabla)}(\mathbf{x},0)=\int_{-\pi}^{\pi}\frac{d^2k}{(2\pi)^2}\left[\frac{1}{(\bar{\mathbf{K}}\cdot\mathbf{K})^2}+\frac{2l^2/a^2}{1+\nu}\frac{1}{\bar{\mathbf{K}}\cdot\mathbf{K}}\right]e^{i\mathbf{k}\cdot\mathbf{x}}=v_4(\mathbf{x})+\frac{2l^2/a^2}{1+\nu}v_2^{(0)}(\mathbf{x}), \tag{25}$$

and that between dislocations by

$$\begin{aligned}v_{ij}^A(\mathbf{x})&=\int_{-\pi}^{\pi}\frac{d^2k}{(2\pi)^2}\left[\frac{\bar{\mathbf{K}}\cdot\mathbf{K}\delta_{ij}-K_i\bar{K}_j}{(\bar{\mathbf{K}}\cdot\mathbf{K})^2}+\frac{2l^2/a^2}{1+\nu}\frac{K_i\bar{K}_j}{\bar{\mathbf{K}}\cdot\mathbf{K}[1+(l^2/a^2)\bar{\mathbf{K}}\cdot\mathbf{K}]}\right]e^{i\mathbf{k}\cdot\mathbf{x}}\\&=[-\bar{\nabla}\cdot\nabla\delta_{ij}-(-\nabla_i\bar{\nabla}_j)]v_4(\mathbf{x})+\frac{2l^2/a^2}{1+\nu}(-\nabla_i\bar{\nabla}_j)[v_2^{(0)}(\mathbf{x})-v_2^{(a/l)}(\mathbf{x})],\end{aligned} \tag{26}$$

where

$$v_2^{(m)}(\mathbf{x})\equiv\int_{-\pi}^{\pi}\frac{d^2k}{(2\pi)^2}\frac{e^{i\mathbf{k}\cdot\mathbf{x}}}{\bar{\mathbf{K}}\cdot\mathbf{K}+m^2} \tag{27a}$$

is the two-dimensional Yukawa potential (which denotes the Coulomb potential, for $m=0$) and

$$v_4(\mathbf{x})\equiv\int_{-\pi}^{\pi}\frac{d^2k}{(2\pi)^2}\frac{e^{i\mathbf{k}\cdot\mathbf{x}}}{(\bar{\mathbf{K}}\cdot\mathbf{K})^2} \tag{27b}$$

with

$$K_i=(e^{ik_i}-1)/i,\quad \bar{K}_i=-(e^{-ik_i}-1)/i,\qquad \bar{\mathbf{K}}\cdot\mathbf{K}\equiv\sum_{i=1}^{2}2(1-\cos k_i). \tag{28}$$

The potentials $v_4$ and $v_2^{(0)}$ are infrared divergent. The divergence is, however, canceled for all defect configurations that are neutral,

$$\sum_{\mathbf{x}}\Theta(\mathbf{x})=0,\quad \sum_{\mathbf{x}}b_i(\mathbf{x})=0,$$

and dipole neutral,

$$\sum_{\mathbf{x}}\mathbf{x}\Theta(\mathbf{x})=0.$$

This condition is automatically fulfilled in the model where the defects arise from defect gauge fields via (15) with periodic boundary conditions. Only these have finite energy. For these one can replace $v_2^{(m)}$ and $v_4$ by the subtracted potentials

$$v_2^{\prime(m)}(\mathbf{x})\equiv\int_{-\pi}^{\pi}\frac{d^2k}{(2\pi)^2}\frac{e^{i\mathbf{k}\cdot\mathbf{x}}-1}{\bar{\mathbf{K}}\cdot\mathbf{K}+m^2}, \tag{29a}$$

$$v_4^{\prime}(\mathbf{x})\equiv\int_{-\pi}^{\pi}\frac{d^2k}{(2\pi)^2}\frac{e^{i\mathbf{k}\cdot\mathbf{x}}-1+(\mathbf{x}^2/4)\bar{\mathbf{K}}\cdot\mathbf{K}}{(\bar{\mathbf{K}}\cdot\mathbf{K})^2}. \tag{29b}$$

On a finite square lattice with periodic boundary conditions, $\int_{-\pi}^{\pi}d^2k/(2\pi)^2$ has to be replaced by $(1/L^2)\sum_{n_1,n_2=0}^{L-1}$, with $\mathbf{k}=(2\pi/L)(n_1,n_2)$.

## IV. THEORETICAL ANALYSIS

Many properties of the phase structure of the model (8) in the $l^2-T(\equiv 1/\beta)$ plane (with $\lambda/\mu$ fixed) can be deduced by mapping appropriate limiting cases onto the well-known Laplacian roughening (LR) model (19) or the discrete Gaussian (DG) model

$$Z_{\mathrm{DG}}\equiv\sum_{\{h\}}\exp\left[-\beta_{\mathrm{DG}}\sum_{\mathbf{x}}(\nabla_i h)^2\right]. \tag{30}$$

Recall the two dually equivalent representations of this model which are (a) the Coulomb gas formulation (analogous to the defect partition function $Z_5$)

$$Z_{\mathrm{DG}}=\mathrm{const}\sum_{\{m\}}\exp\left[-(\pi^2/\beta_{\mathrm{DG}})\sum_{\mathbf{x}}m\frac{1}{-\bar{\nabla}\cdot\nabla}m\right], \tag{31}$$

with $\sum_{\mathbf{x}}m(\mathbf{x})=0$ and the lattice Coulomb potential $(-1/\bar{\nabla}\cdot\nabla)=v_2^{\prime(0)}$. (b) The Villain form of the planar $XY$ model, corresponding to our starting point, the "distortion-plus-defect" model $Z_1$,

$$Z_{\mathrm{DG}}=\text{const}\prod_{\mathbf{x}}\left[\int_{-\pi}^{\pi}d\gamma\right]\sum_{\{n_i\}}\exp\left[-\frac{\beta_v}{2}\sum_{\mathbf{x}}(\nabla_i\gamma-2\pi n_i)^2\right]. \tag{32}$$

The relation between the inverse temperatures of the two representations is $\beta_v=1/(2\beta_{\mathrm{DG}})$.

### A. Phase diagram

#### 1. $l=0$ limit

As already mentioned, the LR model arises by construction as $l=0$ limit of the new model (8). A recent Monte Carlo simulation of the LR model in the dual representation $Z_1^{l=0}$ of Eq. (9) (with $\xi=1$ and $\lambda=0$, for simplicity) indicated a single first-order transition, with clear evidence for metastable states and an entropy jump per site, $\Delta s\approx 0.2$.[4] This happens around

$$\beta_m(1+\nu)=0.815\pm 0.005$$

or

$$\beta_{\mathrm{LR}}^m=\frac{1}{2\beta_m(1+\nu)}=0.613\pm 0.004\ .$$

Hence, from our previous study we know that for $l=0$, the new model (4) undergoes a first-order transition at

$$T_m=\frac{1}{\beta_m}\approx\frac{1+\nu}{0.815}\bigg|_{v=1}=2.454\quad(l=0)\ . \tag{33}$$

It should be noticed, however, that this does not agree with the results of Bruce[5] who claims to see in a simulation of the LR representation (19) a sequence of two continuous transitions at $\beta_{\mathrm{LR}}^{(1)}=0.610$ ($T_{\mathrm{LR}}^{(1)}=1.64$) and $\beta_{\mathrm{LR}}^{(2)}=0.455$ ($T_{\mathrm{LR}}^{(2)}=2.20$). On a triangular lattice, a similar controversy exists.[5,6]

In the opposite limit $l\to\infty$ we have to distinguish two cases.

#### 2. $l\to\infty$, $\beta\sim a^2/l^2\to 0$ ($\beta l^2/a^2$ fixed)

Consider the roughening representation (17). For small $\beta$, the fields $A_i$ are squeezed to zero and (17) becomes effectively a DG model (30) with

$$\beta_{\mathrm{DG}}=\frac{1}{8\beta l^2/a^2}\ , \tag{34}$$

which is well known to undergo a Kosterlitz-Thouless phase transition around

$$\beta_{\mathrm{DG}}^c\approx\beta_{\mathrm{DG}}^{R\,c}=\frac{\pi}{4}=0.785\ , \tag{35}$$

with $\beta_{\mathrm{DG}}^{R\,c}$ denoting the critical renormalized stiffness constant. This rough estimate implies a phase boundary along the line

$$T_2=8(l^2/a^2)\beta_{\mathrm{DG}}^c\approx 2\pi l^2/a^2=6.28l^2/a^2 \tag{36a}$$

separating phases with rough ($T<T_2$) and almost flat ($T>T_2$) $h$-field configurations. Using the more accurate numerical result (see the following and Ref. 21),

$$\beta_{\mathrm{DG}}^c=0.677\pm 0.010\ ,$$

the estimate (36a) can be improved to

$$T_2=(5.42\pm 0.08)l^2/a^2\ . \tag{36b}$$

This phase transition can be deduced also from the defect representation (21) which, in the present limit, reduces to the Coulomb gas representation (31) of the DG model

$$Z_5\to\sum_{\{\Theta\}}\exp\left[-8\pi^2\beta(l^2/a^2)\sum_{\mathbf{x}}\Theta\frac{1}{-\bar{\nabla}\cdot\nabla}\Theta\right]. \tag{37}$$

At large distances, the two-dimensional Coulomb potential $1/(-\bar{\nabla}\cdot\nabla)$ behaves like

$$\frac{1}{-\bar{\nabla}\cdot\nabla}(\mathbf{x},\mathbf{0})\equiv v_2^{\prime(0)}(\mathbf{x})\xrightarrow[|\mathbf{x}|\to\infty]{}-\frac{1}{2\pi}\ln(2\sqrt{2}e^{\gamma}|\mathbf{x}|)\ , \tag{38}$$

where $\gamma\approx 0.5772$ is Euler's constant. The standard renormalization-group analysis[2] shows that the effect of few bound defects at low temperatures can effectively be taken into account by replacing $\beta$ by a renormalized stiffness constant $\beta^R$. This simple picture breaks down when the prefactor of the logarithmic potential in (37) becomes 2, i.e., if $4\pi\beta_2^R l^2/a^2=2$. Thus there is a pair-unbinding transition at

$$\beta_2^R=\frac{1}{2\pi l^2/a^2} \tag{39}$$

or, using (34), $\beta_{\mathrm{DG}}^{R\,c}=\pi/4$. We see that in rotationally stiff material (large $l$), higher temperatures are needed to produce free, unbound disclinations. Approximating $\beta\approx\beta_2^R$, one arrives at the estimate (36a).

#### 3. $l\to\infty$, $\beta\approx 1$

Consider again first the roughening representation (17). For $\beta\approx 1$ and $l^2\to\infty$, the field $h$ can be treated effectively as continuous and integrated out, yielding

$$Z_4 \to \sum_{\{A_i\}} \exp\left\{-\frac{1}{\beta}\sum_{\mathbf{x}}\left[\frac{1}{4}\left[\frac{1}{1+\nu}(\overline{\nabla}_i A_j)^2-\frac{1}{2}\frac{1-\nu}{1+\nu}(\overline{\nabla}_i A_i)^2\right]+\frac{a^2}{8l^2}A_i\frac{1}{-\overline{\nabla}\cdot\nabla}(-\nabla_i\overline{\nabla}_j)A_j+\cdots\right]\right\}. \tag{40}$$

For *infinite l*, the last term with the nonlocal corrections vanishes and we end up with a discrete Gaussian vector model which, for $\nu=1$ (incompressible material), decouples into two ordinary DG models with an inverse temperature

$$\beta_{\mathrm{DG}}=\frac{1}{8\beta}\ , \tag{41}$$

implying a Kosterlitz-Thouless transition at

$$T_1=8\beta_{\mathrm{DG}}^c=5.42\pm0.08\approx 2\pi=T_1^R \quad (\nu=1,\ l=\infty)\ . \tag{42}$$

For any *finite l*, however, the nonlocal corrections in (40) become important at long distance and, in fact, reduce the transition temperature by a factor of about 2 (for $\nu=1$). This is most easily seen in the defect representation (21), which becomes effectively, for large but finite $l$,

$$Z_5 \to \sum_{\{b_i\}} \exp\left[-4\pi^2\beta(1+\nu)\sum_{\mathbf{x}} b_i v_{ij}'^A b_j\right]\ , \tag{43}$$

where the dislocation potential (26) can be taken in the regularized form

$$v_{ij}'^A(\mathbf{x})=\int_{-\pi}^{\pi}\frac{d^2k}{(2\pi)^2}\left[\frac{\overline{\mathbf{K}}\cdot\mathbf{K}\delta_{ij}-K_i\overline{K}_j}{(\overline{\mathbf{K}}\cdot\mathbf{K})^2}+\frac{2l^2/a^2}{1+\nu}\frac{K_i\overline{K}_j}{\overline{\mathbf{K}}\cdot\mathbf{K}[1+(l^2/a^2)\overline{\mathbf{K}}\cdot\mathbf{K}]}\right](e^{i\mathbf{k}\cdot\mathbf{x}}-1)\ , \tag{44}$$

since only neutral dislocation configurations $\sum_{\mathbf{x}} b_i=0$ give a finite contribution. For any finite $l$, the subtraction in the second term is not really necessary, but does no harm and ensures a finite $l=\infty$ limit.

Asymptotically as $|x|\to\infty$, the second term contributes only minor corrections since, for any finite $l$, it behaves like $[2l^2/a^2/(1+\nu)]\,(K_i\overline{K}_j/\overline{\mathbf{K}}\cdot\mathbf{K})$ as $k\to 0$. Only in the singular limit of *infinite l* it becomes

$$[2/(1+\nu)][K_iK_j/(\overline{\mathbf{K}}\cdot\mathbf{K})^2]\approx[2/(1+\nu)](1/k^2)$$

and does contribute to the asymptotic behavior. For $\nu=1$, this combines with the first term to a Coulomb potential

$$v_{ij}'^A(\mathbf{x})=\int_{-\pi}^{\pi}\frac{d^2k}{(2\pi)^2}\frac{\delta_{ij}}{\overline{\mathbf{K}}\cdot\mathbf{K}}(e^{i\mathbf{k}\cdot\mathbf{x}}-1)=\delta_{ij}v_2'^{(0)}(\mathbf{x}) \quad (\nu=1,\ l=\infty)$$

$$\xrightarrow[|\mathbf{x}|\to\infty]{} -\frac{1}{2\pi}\ln|\mathbf{x}|\delta_{ij} \tag{45}$$

and thus leads to the ordinary DG transition given in (41) and (42). For general $\nu$, we have at $l=\infty$ the subtracted potential between dislocations

$$v_{ij}'^A(\mathbf{x})=\int_{-\pi}^{\pi}\frac{d^2k}{(2\pi)^2}\frac{\overline{\mathbf{K}}\cdot\mathbf{K}\delta_{ij}-K_i\overline{K}_j+[2/(1+\nu)]K_i\overline{K}_j}{(\overline{\mathbf{K}}\cdot\mathbf{K})^2}(e^{i\mathbf{k}\cdot\mathbf{x}}-1)$$

$$=\left[-(\overline{\nabla}\cdot\nabla\delta_{ij}-\nabla_i\overline{\nabla}_j)-\frac{2}{1+\nu}\nabla_i\overline{\nabla}_j\right]v_4''(\mathbf{x})\ . \tag{46}$$

From the asymptotic behavior of $v_4''$ (Ref. 16),

$$v_4''(\mathbf{x})\xrightarrow[|\mathbf{x}|\to\infty]{}\frac{1}{8\pi}[\mathbf{x}^2\ln(2\sqrt{2}e^{\gamma-1}|\mathbf{x}|)-\tfrac{1}{2}\ln(2\sqrt{2}e^{\gamma-1/6}|\mathbf{x}|)]\ , \tag{47}$$

we calculate

$$v_{ij}'^A(\mathbf{x})\xrightarrow[|\mathbf{x}|\to\infty]{}-\left[\left[\frac{1}{2\pi}-\frac{1}{4\pi}\right]+\frac{1}{2\pi(\nu+1)}\right]\ln|\mathbf{x}|\delta_{ij}=-\frac{1}{4\pi}\left[1+\frac{2}{1+\nu}\right]\ln|\mathbf{x}|\delta_{ij}\ . \tag{48}$$

The factors are obvious by replacing approximately $\overline{\nabla}\cdot\nabla$ by $\partial^2$ and $\overline{\nabla}_i\nabla_j$ by $\frac{1}{2}\delta_{ij}\partial^2$. Applying the Coulomb gas criterion as in (37)–(39), this gives

$$T_1\approx T_1^R=\pi[(1+\nu)+2]/2 \quad (l=\infty)\ , \tag{49}$$

in agreement with (42) for $\nu=1$. The 2 inside the square brackets is due to the longitudinal modes in (46).

For the physical case of *finite l*, on the other hand, the longitudinal modes in (46) have finite range $\propto l$ and thus do not contribute to the asymptotic behavior. The phase transition is therefore determined alone from the transversal

modes, for which the potential (46)–(48) is, at any $\nu$,

$$v_{ij}'^{A}(\mathbf{x}) \xrightarrow[|\mathbf{x}|\to\infty]{} \int_{-\pi}^{\pi} \frac{d^2k}{(2\pi)^2} \frac{\overline{\mathbf{K}}\cdot\mathbf{K}\delta_{ij}-K_i\overline{K}_j}{(\overline{\mathbf{K}}\cdot\mathbf{K})^2}(e^{i\mathbf{k}\cdot\mathbf{x}}-1) = -(\overline{\nabla}\cdot\nabla\delta_{ij}-\nabla_i\overline{\nabla}_j)v_4''(\mathbf{x}) \xrightarrow[|\mathbf{x}|\to\infty]{} -\frac{1}{4\pi}\ln|\mathbf{x}|\delta_{ij} \ . \tag{50}$$

This yields the transition temperature

$$T_1 \approx T_1^R = \pi(1+\nu)/2|_{\nu=1} = \pi \quad (l \text{ finite}) \ . \tag{51}$$

Compared with the $l=\infty$ value (42) we see that the screening of the longitudinal modes at large distance has reduced the transition temperature $T_1$ for $\nu=1$ by a factor of about 2. Let us recall that according to the renormalization-group equations the distance between the renormalized critical temperature $T_1^R$ and the actual transition temperature $T_1$ decreases rapidly with the fugacity of the excitations. Since the core energy $\varepsilon_{\text{core}}$ of the excitations is only weakly dependent on $l$, the fugacity $y \equiv e^{-\varepsilon_{\text{core}}/T}$ near the $l=\infty$ transition temperature $T_1 \approx 2\pi$ is much larger than at $T_1 \approx \pi$ for finite $l$. This is why the approximation (51) is much more accurate than (42). Consequently, the actual transition temperatures for $l=\infty$ and $l=$finite differ only roughly by a factor of 2. Via the fugacity, $T_1$ is only weakly dependent on $l$. This is physically expected since the unbinding transition of dislocation pairs, the *translational* defects, should be only weakly influenced by the length scale $l$ of *rotational* stiffness.

In Fig. 1 the theoretically predicted phase diagram in the $l^2$-$T$ plane for $\nu=1$ is compared with the results of our Monte Carlo simulations to be described in Sec. IV B. In the diagram we have tentatively identified the three phases according to their defect structures as solid, hexatic, and liquid, although we have not yet performed any detailed structural investigations to confirm these phase properties.

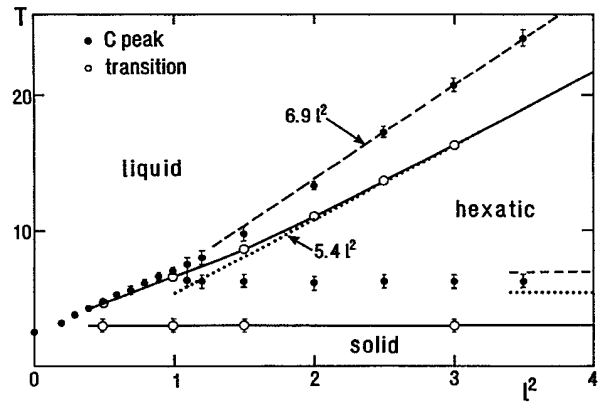


FIG. 1. The $l^2$-$T$ phase diagram of the lattice-defect melting model for $\nu=1$. The transition points (0) are determined from measurements of correlation functions on $32\times32$ lattices. For $l^2 \gtrsim 1$, they lie significantly lower in temperature than the location of the finite specific-heat peaks (●), as expected for Kosterlitz-Thouless-like transitions. The dashed and dotted straight lines are calculated from the $l\to\infty$ limit in which the melting model degenerates at both transitions to a pure DG model. At the lower transition, the $l=\infty$ transition temperature is higher by a factor of about 2 due to a subtlety discussed in the text. The solid lines are a guide to the eye.

### B. Correlation functions

Numerically, the phase diagram can be mapped out by measuring appropriate correlation functions. Since we have chosen to work with the roughening picture (17), we shall discuss only the height-height correlation functions

$$\tfrac{1}{2}\langle[h(\mathbf{x})-h(\mathbf{x}')]^2\rangle = \langle h(\mathbf{x})^2\rangle - \langle h(\mathbf{x})h(\mathbf{x}')\rangle \tag{52a}$$

and

$$\tfrac{1}{2}\langle[A_i(\mathbf{x})-A_j(\mathbf{x}')]^2\rangle \ , \tag{52b}$$

where the angular brackets denote thermal averages with respect to $Z_4$ of Eq. (17). In the following we shall assume large enough $l$ to avoid degenerate cases. Let us start by showing that, in the low-temperature solid phase, these functions are proportional to the defect potentials given in (24)–(26). For low temperatures, there are only few defects, and the discrete variables $h$, $A_1$ can be treated effectively as massless continuous fields. The dilute gas of bound defects (which is caused by the integerness of the fields $h$, $A_i$) manifests itself only in a renormalization of the temperature, i.e., $\beta\to\beta^R$. This effect is exponentially small because of the finite activation energies, i.e., low fugacities. Omitting in $Z_3$ of Eq. (14) the sum over defects and interpreting $2\pi\Theta$ and $2\pi b_i$ as fixed external sources, the correlations (52) may be generated by differentiation with respect to these sources. Applying these differentiations then to the dual defect representation $Z_5$ of Eq. (21) (and replacing $\beta\to\beta^R$), it is easy to read off [using (24)]

$$\tfrac{1}{2}\langle[h(\mathbf{x})-h(\mathbf{x}')]^2\rangle = -4\beta^R\frac{1+\nu}{2}[v^h(\mathbf{x}-\mathbf{x}')-v^h(\mathbf{0})] \ , \tag{53a}$$

$$\tfrac{1}{2}\langle[A_i(\mathbf{x})-A_j(\mathbf{x}')]^2\rangle = -4\beta^R\frac{1+\nu}{2}v_{ij}'^{A}(\mathbf{x}-\mathbf{x}') \ , \tag{53b}$$

with $v^h$ and $v_{ij}'^{A}$ given in (25) and (44), respectively. Note that in the solid phase (which is extremely rough in the dual picture) $\langle[h(\mathbf{x})-h(\mathbf{0})]^2\rangle$ diverges for all $\mathbf{x}$ as $\ln V$, where $V=L\times L$ is the lattice volume.

Then, with increasing temperature, we expect at the first phase transition around $T_1 \approx \pi$ the $A$ correlations to become effectively massive as a two-dimensional disorder version of the Meissner effect in superconductivity.[17] In the roughening language this corresponds to almost constant fields $A$. As a consequence, in the intermediate phase the $h$ correlations are screened at long range to

$$\tfrac{1}{2}\langle[h(\mathbf{x})-h(\mathbf{x}')]^2\rangle=-4\beta^R(l^2/a^2)v_2'^{(0)}(\mathbf{x}-\mathbf{x}')\ , \tag{54}$$

which is exactly the behavior in the massless phase of the DG model, where the field $h$ is still rough.

When increasing the temperature further then, at the second transition around $T_2\approx 5.42l^2/a^2$, also the $h$ correlations become massive corresponding to a phase with almost constant fields $A$ and $h$.

Since each phase is characterized by a special behavior of the correlation functions (52), it is at least in principle straightforward to map out the phase diagram. In an actual Monte Carlo simulation this can be quite time consuming since one needs large lattices and very good statistics to disentangle the different asymptotic behaviors. It is therefore quite important to find related correlations that can be measured and analyzed more efficiently. We have chosen to study the projected correlation functions

$$c^h(x-x')\equiv\frac{L}{2}\langle[\bar{h}(x)-\bar{h}(x')]^2\rangle$$
$$=L[\langle\bar{h}(x)^2\rangle-\langle\bar{h}(x)\bar{h}(x')\rangle]\ , \tag{55}$$

and

$$c_{ij}^A(x-x')\equiv\frac{L}{2}\langle[\bar{A}_i(x)-\bar{A}_j(x')]^2\rangle\ , \tag{56}$$

where $L$ is the linear size of the square lattice, and the bars denote a configuration average along one column (or row), e.g.,

$$\bar{h}(x)=\frac{1}{L}\sum_{y=1}^{L}h(x,y)\ .$$

In momentum space, these averages amount to a projection onto the $k_1$ axis [$\mathbf{x}=(x,y)$, $\mathbf{k}=(2\pi/L)(n_x,n_y)$]:

$$\frac{1}{L^2}\sum_{y,y'}f(\mathbf{x}-\mathbf{x}')\equiv\frac{1}{L^2}\sum_{y,y'}\frac{1}{L^2}\sum_{n_x,n_y=0}^{L-1}f(k_x,k_y)e^{i\mathbf{k}\cdot(\mathbf{x}-\mathbf{x}')}$$
$$=\frac{1}{L}\frac{1}{L}\sum_{n_x=0}^{L-1}f(k_x,0)e^{ik_x(x-x')}\ . \tag{57}$$

This leads to simple one-dimensional representations for $c^h(x)$ and $c_{ij}^A(x)$ which, in the free field case, can be evaluated analytically even on finite lattices (see the Appendix). Applying these projections to (53) we get in the low-temperature solid phase

$$c^h(x)=-4\beta^R\frac{1+\nu}{2}\left[c_4(x)+\frac{2l^2/a^2}{1+\nu}c_2^{(0)}(x)\right]\ , \tag{58}$$

where $c_2^{(m)}$ and $c_4$ are the one-dimensional versions of $v_2^{(m)}$ and $v_4$ [compare (27) and see the Appendix]. The projections of $v_{ij}'^A$ result in $c_{12}^A=c_{21}^A=0$ and

$$c^{A_1}(x)\equiv c_{11}^A(x)=-4\beta^R c_2^{(a/l)}(x)\ , \tag{59}$$

$$c^{A_2}(x)\equiv c_{22}^A(x)=-4\beta^R\frac{1+\nu}{2}c_2^{(0)}(x)\ . \tag{60}$$

In the intermediate phase, we find from (54)

$$c^h(x)=-4\beta^R(l^2/a^2)c_2^{(0)}(x)\ . \tag{61}$$

The $A$ correlations are massive in this phase.

## V. NUMERICAL ANALYSIS

### A. The Monte Carlo simulation

As discussed in Sec. II, the new lattice defect model allows for several equivalent representations, and it is not at all obvious which one is best suited for simulations. The situation is completely analogous to the much simpler (planar) $XY$ model, where the same sequence "distortion-plus-defect," "roughening," and "defect gas" representation is found. In this simpler case, all three representation have been studied by Monte Carlo methods. The "defect gas" representation has the most obvious physical interpretation but is, unfortunately, quite tedious to simulate. Also the "distortion-plus-defect" representation has a very close relation to the melting process, and, furthermore, it is possible to extract the defect information by simple algebraic manipulations.[4,7] In the interesting low-temperature phase it is, however, quite difficult to extract well equilibrated thermal averages. In the dual roughening representation this corresponds to the hot phase with very rough configurations where no equilibration problems occur. The obvious disadvantage is, of course, the loss of a direct interpretation in terms of displacements of atoms or in terms of crystalline defects. In fact, since the transformation from (8) to (14) involves a change of integration (field) variables, it is only true after summing over *all* configurations. This makes it impossible to extract from a given surface configuration the corresponding defect configuration. Nevertheless, in this work we have used the roughening representation because of its numerical advantages. This choice was also influenced by the fact that the "distortion-plus-defect" representation (8) for $l\neq 0$ is much more involved than for $l=0$, where we actually used it.[4,7] In the $l=0$ case (with $\lambda/\mu=0$) the summations over integers $N_{12}$, $N_{11}$, and $N_{22}$ in (9) factorize and can be done locally at each lattice site with any desired accuracy. The Monte Carlo simulation involves then only the $\gamma$ degrees of freedom

$$Z_1^{l=0}=\prod_{\mathbf{x}}\left[\int_{-\pi}^{\pi}d^2\gamma\right]\exp\left[-\sum_{\mathbf{x}}V\left(\frac{\beta}{2},\nabla_1\gamma_2+\nabla_2\gamma_1\right)\right.$$
$$\left.-\sum_{\mathbf{x},i}V(\beta\xi,\nabla_i\gamma_i)\right]\ , \tag{62}$$

where

$$e^{-V(x,\Theta)}\equiv\sum_n e^{-x(\Theta-2\pi n)^2}\ . \tag{63}$$

For $l\neq 0$ this is no longer possible and we resorted to the roughening representation (17).

To update the integer valued configurations, we applied the standard Metropolis algorithm with trial values for $h(\mathbf{x})$ and $A_i(\mathbf{x})$ chosen randomly from one above or one below the current value at each site. In all simula-

tions periodic boundary conditions were used.

### B. Numerical results

The main results of our Monte Carlo study are summarized in Fig. 1, which shows the $l^2$-$T$ phase diagram for $\nu=1$. We determined the transition points by measuring first specific heats, for an estimate, and afterwards correlation functions, for a precise determination.

#### 1. Specific heats

Let us start with a discussion of the specific-heat curves that serve at least for a *rough* estimate of the phase boundaries. We emphasize rough since we expect Kosterlitz-Thouless transitions in part of the phase diagram, and it is well known that in this case transition point and peak position of the specific heat do not agree. For $\nu=1$, the partition function reduces to

$$Z_4=\sum_{\{A_i h\}}\exp\left[-\frac{1}{8\beta}\sum_{\mathbf{x}}\left[(\bar{\nabla}_i A_j)^2+\frac{1}{l^2/a^2}(\bar{\nabla}_i h-\epsilon_{ij}A_j)^2\right]\right] . \tag{64}$$

It is convenient to use $\beta'_{\mathrm{DG}}=1/8\beta=T/8$ as basic parameter and define the internal energy as

$$e\equiv\langle u\rangle=\langle U\rangle/L^2=-\frac{1}{L^2}\frac{\partial}{\partial\beta'_{\mathrm{DG}}}\ln Z_4=\left\langle\frac{1}{L^2}\sum_{\mathbf{x}}\left[(\bar{\nabla}_i A_j)^2+\frac{1}{l^2/a^2}(\bar{\nabla}_i h-\epsilon_{ij}A_j)^2\right]\right\rangle . \tag{65}$$

The specific heat is then defined as

$$c=C/L^2=-\beta'^2_{\mathrm{DG}}\frac{\partial\langle u\rangle}{\partial\beta'_{\mathrm{DG}}}=\beta'^2_{\mathrm{DG}}L^2(\langle u^2\rangle-\langle u\rangle^2) . \tag{66}$$

Our measurements of the specific heat are all based on the energy fluctuations on the right-hand side (rhs) of (66).

As pointed out before, for $l^2\to\infty$ and $\beta\approx 1$, near the first transition, the $h$ fields can be effectively integrated out, leading to

$$Z_4\approx\text{const}\exp\left[-\frac{L^2}{2}\ln\beta'_{\mathrm{DG}}\right]Z_{\mathrm{DG}}(\beta'_{\mathrm{DG}})^2 . \tag{67}$$

Here, we have neglected all non-local corrections $\sim a^2/l^2$. From this we read off

$$\left\langle\frac{1}{L^2}\sum_{\mathbf{x}}(\bar{\nabla}_i A_j)^2\right\rangle\approx 2e_{\mathrm{DG}} , \tag{68}$$

$$\left\langle\frac{a^2}{l^2}\frac{1}{L^2}\sum_{\mathbf{x}}(\bar{\nabla}_i h-\epsilon_{ij}A_j)^2\right\rangle\approx\frac{1}{2\beta'_{\mathrm{DG}}}=\frac{4}{T} , \tag{69}$$

so that near the first transition

$$e\approx 2e_{\mathrm{DG}}+\frac{4}{T} , \tag{70}$$

$$c\approx 2c_{\mathrm{DG}}+\tfrac{1}{2} . \tag{71}$$

For $l^2\to\infty$ and $\beta\sim a^2/l^2\to 0$, the partition function becomes effectively

$$Z_4\approx Z_{\mathrm{DG}}(\beta_{\mathrm{DG}}) , \tag{72}$$

where

$$\beta_{\mathrm{DG}}=\beta'_{\mathrm{DG}}/(l^2/a^2)=\frac{1}{8\beta l^2/a^2} .$$

Therefore, near the second transition

$$e\approx\frac{1}{l^2/a^2}e_{\mathrm{DG}}(\beta_{\mathrm{DG}}) , \tag{73}$$

$$c\approx c_{\mathrm{DG}}(\beta_{\mathrm{DG}}) . \tag{74}$$

Since $T=8(l^2/a^2)\beta_{\mathrm{DG}}$ is proportional to $l^2$, the peak of $c$ becomes broader with increasing $l^2$ when plotted against $T$.

For $l^2\to 0$, the model reduces to the LR model

$$Z_4\approx Z_{\mathrm{LR}}(\beta_{\mathrm{LR}}) , \tag{75}$$

with $\beta_{\mathrm{LR}}=1/4\beta$ so that

$$e\approx 2e_{\mathrm{LR}}(\beta_{\mathrm{LR}}) , \tag{76}$$

$$c\approx c_{\mathrm{LR}} . \tag{77}$$

Let us now describe the results of our Monte Carlo simulations. From now on we shall use natural units in which $a\equiv 1$ (=lattice spacing). In Fig. 1, the peak positions are shown as solid circles. Most of them were determined on $16\times 16$ lattices at fixed $l^2$ by first running a relatively fast thermal cycle over a wide temperature range (see Fig. 2), and then by studying the tips of the peaks with much higher statistics. At each temperature, in the fast runs we used 5000 configurations for thermal averages, after discarding 1000 configurations for equilibration. In the long runs we increased these parameters by a factor 50 to 250 000 and 50 000, respectively, thus reducing the statistical errors by about a factor 7. For an estimate of these errors we applied the usual blocking procedure, recording blocks of different lengths to make sure that the "Monte Carlo time" correlation length was much smaller than the length of the blocks used for the final estimates. The results for the peak positions are compiled in Table I (see also Fig. 2). For a few selected values of $l^2$, we have also studied the finite-size scaling behavior of the specific-heat peaks with increasing lattice size. Our results for $l^2=0.5$, 1, and 3 are shown in Fig. 3. At $l^2=3$, the peaks associated with the two transitions (compare with Fig. 1) show almost no finite-size dependence as expected for Kosterlitz-Thouless type transitions. In fact, the data for the high-temperature peak

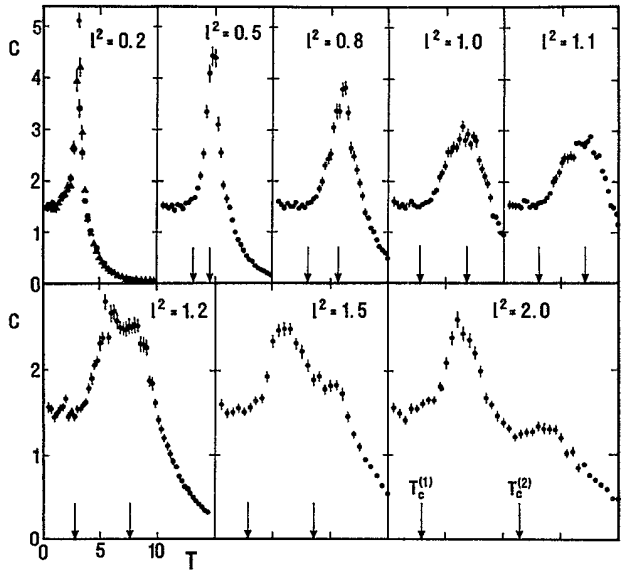


FIG. 2. The specific heat vs temperature on a $16\times16$ lattice with increasing length scale $l$ of rotational stiffness. The data are averages over 5000 configurations, after discarding 1000 configurations for thermalization. In all plots, the temperature scale is the same. The arrows indicate the transition points determined from measurements of correlation functions. For $l^2\gtrsim1$, they are clearly displaced to lower temperatures, compared with the peaks.

[Fig. 3(b)] are almost identical with those of the (properly rescaled) DG model shown as solid ($L=16$) and dotted ($L=8$) lines, respectively. For the position of the peak in the DG model, we estimate (using a parabolic fit, see Fig. 4)

$$\beta_{\rm DG}^{\rm peak}=0.861\pm0.005\ , \tag{78a}$$

which translates to

$$T_2^{\rm peak}\approx 8l^2\beta_{\rm DG}^{\rm peak}=(6.89\pm0.04)l^2\ . \tag{78b}$$

For $l^2=3$, this gives $20.67\pm0.12$, in perfect agreement with the direct estimate for this $l^2$ (compare Table I). For smaller $l^2$, we find values for $T_2^{\rm peak}$ that are somewhat lower than those predicted by the DG model approximation. Also the shape of the peaks deviates with decreasing $l^2$ more and more from the DG curve, as can be inspected in Fig. 4. Let us now turn to the low-temperature peak [Fig. 3(a)], which shows also almost no finite-size dependence. It is, however, still somewhat displaced with respect to the ideal $l^2\to\infty$ limit, which is again the DG model. We have checked that for larger $l^2(\approx10,\ldots,50)$, the peak position moves slowly upward to

$$T_1^{\rm peak}\approx 8\beta_{\rm DG}^{\rm peak}=6.89\pm0.04\ , \tag{78c}$$

confirming the above expectation. For $l^2=1$ [Fig. 3(c)], there is only a single peak showing small size dependence. At $l^2=0.5$ [Fig. 3(d)], we observe small but sizable size dependence, which, however, seems to saturate at reasonably small $L$. Summarizing, we see that down to $l^2\approx0.5$ the specific-heat peaks show only a very weak size dependence, and we conclude that the transitions are good candidates for the Kosterlitz-Thouless type.

This picture changes dramatically at $l^2=0.2$. The specific heat displayed in Fig. 5 shows a clear finite-size scaling behavior typical for a low-order phase transition, possibly a first-order one. The speculation on the order of the transition is born out mainly from a parallel study

TABLE I. Locations of the specific-heat peaks in the high-temperature transition.

| $l^2$ | $T_2^{\rm peak}$ | $T_2^{\rm peak}(l^2/3)$ |
|---|---|---|
| 1.5 | 9.75±0.50 | 19.5±1.0 |
| 2 | 13.33±0.33 | 20.0±0.5 |
| 2.5 | 17.30±0.40 | 20.75±0.5 |
| 3.0 | 20.75±0.50 | 20.75±0.5 |
| 3.5 | 24.21±0.60 | 20.75±0.5 |

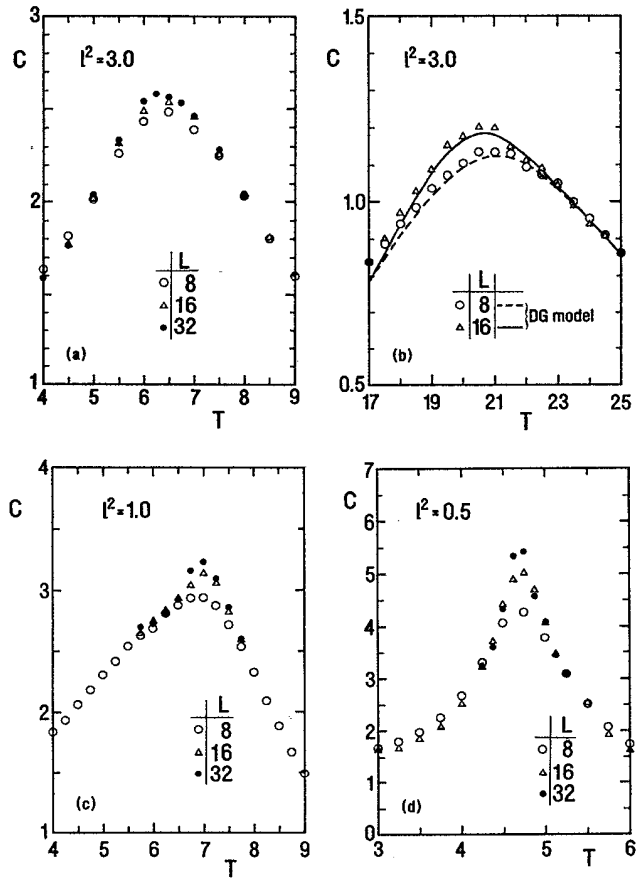


FIG. 3. Scaling behavior of the specific-heat peaks with lattice size $L$ for decreasing length scale $l$ of rotational stiffness. (a) and (b) For $l^2=3$, the peaks at the low- and high-temperature transition are both almost size independent, as expected for Kosterlitz-Thouless transitions. The solid and dashed curves in (b) show properly rescaled fits to data of the pure DG model. (c) and (d) For decreasing $l^2$, the finite-size scaling becomes more pronounced, indicating a crossover to a first-order transition for small $l^2$.

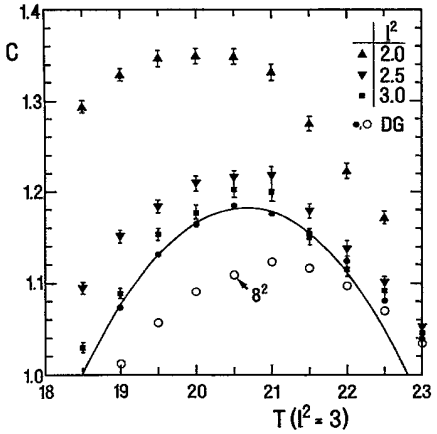


FIG. 4. Approach of the DG model limit (●) of the specific heat at $l^2 \to \infty$ on a $16 \times 16$ lattice. For an easier comparison, we have moved the peak locations near to each other by rescaling the temperature axis for $l^2=2.0$ and $l^2=2.5$ with a factor $3/l^2$. The continuous line is a parabolic fit, $c=a+b(T-T^{\text{peak}})^2$, through the five DG model points in the range $T=19.5$–$21.5$ with $a=1.182$, $b=-0.039$, and $T^{\text{peak}}=20.65$ ($\beta_{\text{DG}}^{\text{peak}}=T^{\text{peak}}/24=0.8605$).

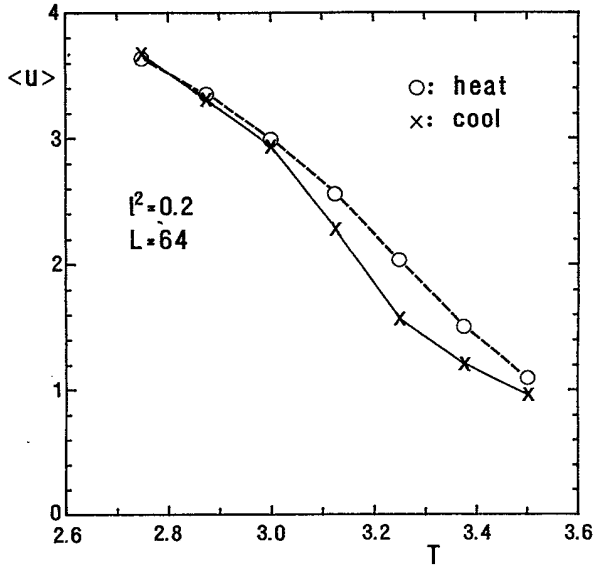


FIG. 6. Internal energy vs temperature for $l^2=0.2$ on a $64 \times 64$ lattice. The stability of the hysteresis, even for long runs with 12 000 sweeps per data point (the last 10 000 are used for averages), supports the hypothesis of a crossover to first-order transitions for $l^2 \lesssim 0.2$.

of the internal energy: It shows (a) a clear hysteresis in relatively slow thermal cycles (see Fig. 6), and (b) near the estimated transition temperature the time evolutions of runs starting with "hot" or "cold" configurations show stable behavior over very many sweeps. It must be noted, however, that although the peak height of the specific heat scales quite strongly with $L$, it does not really reach the behavior $c_{\max} \sim$ volume, expected for a first-order transition. A possible explanation is that we have not yet reached the asymptotic region that might set in only at quite large $L$. A similar behavior has been recently seen[6] in the $l=0$ limit, the Laplacian roughening model, and, in general, for many other models with *weak* first-order transitions (e.g., the $q=5$ Potts model in two dimensions).

In any case, the strong size dependence of the specific heat seems to exclude a Kosterlitz-Thouless transition at $l^2=0.2$.

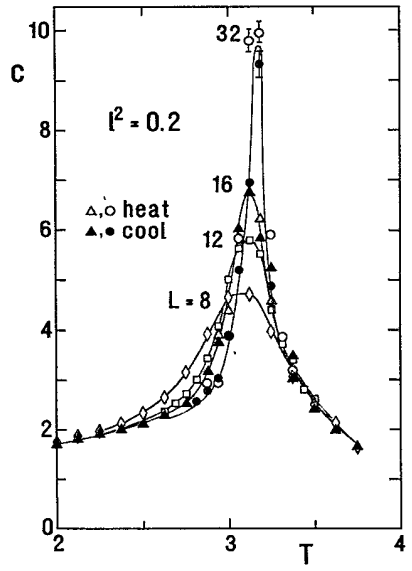


FIG. 5. Finite-size scaling behavior of the specific-heat peak for $l^2=0.2$. The pronounced size dependence does not support a transition of the Kosterlitz-Thouless type. On the contrary, it suggests a crossover to first-order transitions in this range of $l^2$.

### 2. *Comparative study of correlation functions in DG model*

Let us now turn to the discussion of the correlation functions that will add additional information, confirming and completing the overall picture derived so far. To start, we have performed a comparative study of the ordinary DG model that may serve as "gauge system," while analyzing the new model. As already mentioned earlier, the DG model has been studied in several representations, so that there are enough sources for comparison. There is, of course, still another motivation for reanalyzing the DG model: A recent study[18] of the (planar) $XY$ model using projected correlation functions has indicated a value for $\beta_{xy}^c$ being quite different from older estimates based on measurements of two-dimensional correlations.[19] Since the planar model is mapped very accurately onto the dual version of the DG model by a Villain approximation,[20] it is interesting to investigate whether the old estimates of $\beta_{\text{DG}}^c$, which are also extracted from the behavior of two-dimensional correlations, can be reproduced using the projection technique.

The results of our simulations on $32 \times 32$, $48 \times 48$, and $64 \times 64$ lattices are shown in Fig. 7. In Fig. 7(a), we have plotted for the $64 \times 64$ lattice the raw data of $c^h(x)$ versus

$x$ in the massless phase. Here the temperature $T$ is related to $\beta_{DG}$ via $\beta_{DG}=T/24$ [corresponding to $l^2/a^2=3$ in (34)]. The continuous curves are fits to the expected behavior in the massless phase,

$$c^h(x)=-\frac{1}{2\beta^R_{DG}(\beta)}c_2^{(0)}(x)+\text{const}\ , \tag{79}$$

yielding directly the renormalized stiffness constant $\beta^R_{DG}(\beta)$. The offset turned out to be approximately zero, indicating that the asymptotic behavior $\sim c_2^{(0)}(x)$ is correct to surprisingly small distances—there are almost no finite lattice spacing corrections.

In Fig. 7(b), we apply a finite-size scaling test for a vanishing mass ($\hat{=}$infinite correlation length). For vanishing mass the system is scale invariant, and this in turn implies that all data for $c^h(x)/L$, when plotted versus $x/L$, should fall onto a universal curve independent of $L$. [Assuming the ansatz (79) with const=0, this can be checked explicitly.] We see that this expectation is clearly satisfied for $T\lesssim 16$. For $T=16.5$, the data for $L=32$ and $L=48$ still fit quite well, while the data for $L=64$ lie systematically lower, indicating an inverse mass (=correlation length) around $48,\ldots,64$. For $T>17$, the sys-

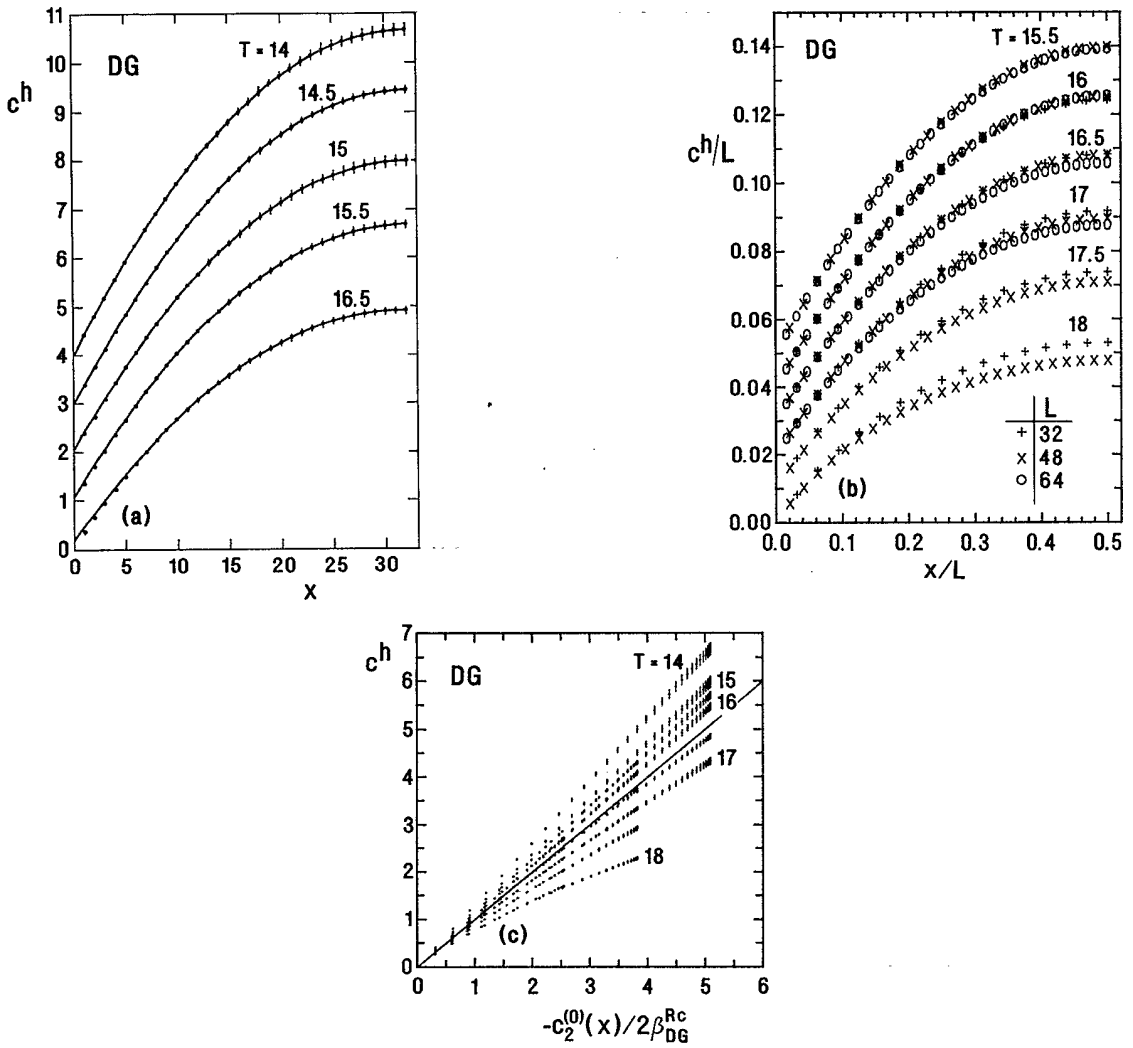


FIG. 7. (a) Projected correlation functions $c^h(x)$ vs $x$ in the massless phase of the DG model on a $64\times 64$ lattice. In order to disentangle the curves for different temperatures they are shifted by a constant (=1). The continuous curves are fits to the theoretical prediction $c^h(x)=-[1/2\beta^R_{DG}(\beta)]c_2^{(0)}(x)+\text{const}$, where $\beta^R_{DG}(\beta)$ is the renormalized stiffness constant and $c_2^{(0)}(x)=-(x/2)(1-x/L)$ is the one-dimensional massless potential calculated in the Appendix. (b) Finite-size scaling plot of projected correlation functions $c^h(x)$ of the DG model on $32\times 32$ (+), $48\times 48$ ($\times$), and $64\times 64$ ($\circ$) lattices. In order to disentangle the curves for different temperatures they are shifted by a constant (=0.01). In the massless phase ($T\lesssim 16.25$), the data for the different lattices collapse onto a single curve. In the massive phase ($T\gtrsim 16.25$), on the other hand, we observe a systematic dependence on the lattice size, becoming stronger with increasing temperature. This qualitative change is a clear signal for a phase transition at $T_c\approx 16.25(\beta^c_{DG}=T_c/24\approx 0.677)$. (c) Projected correlations $c^h(x)$ of the DG model vs the massless propagator $-c_2^{(0)}(x)/2\beta^{R\,c}_{DG}$ with $\beta^{R\,c}_{DG}=\pi/4$ [see Eq. (35)]. Shown are data for $L=64$, as well as $L=48$ and $L=32$ (with limiting points at $x$ values $\approx 4$ and $\approx 2.5$, respectively). The straight line is the critical slope for $T=T_c\approx 16.25$, separating the massless and massive phases. In the massless phase ($T<T_c$), the data are well fitted by straight lines. In the massive phase ($T>T_c$), a downward curvature is clearly visible.

tematic size dependence becomes more and more pronounced. Not that such a test for the massless phase does not assume any explicit form for $c^h(x)$ as input. The disadvantage is the need of data on different lattice sizes, which is of course very time consuming for more complicated models.

We have therefore tried yet another way of presenting the data in an informative way, namely by plotting $c^h(x)$ versus the expected asymptotic behavior $-c_2^{(0)}(x)/(2\beta_{\rm DG}^{R\,c})$. In such a plot, we expect in the massless phase straight lines with a minimal critical slope equal to 1 (provided that we have scaled the $x$ axis by the renormalized stiffness constant $\beta_{\rm DG}^{R\,c}=\pi/4$). In the massive phase, on the other hand, the data should show a downward curvature at large distances. If the lattice size is smaller than the inverse mass (=correlation length), this curvature is hardly detectable, but the slope of the apparently straight line will be smaller than the critical slope. This is demonstrated in Fig. 7(c), where we have plotted our data for $L=64$ as well as for $L=48$ and $L=32$ (which can be traced by the limiting points around $x$ values $\approx 4$ and $\approx 2.5$). For $T\leq 16$, the curves are indeed straight lines with slope $>1$. For $T=16.5$, on the $64\times 64$ lattice a small downward curvature is detectable that is hardly seen on the smaller lattices [compare the scaling plot Fig. 7(b)]. The slope, however, is seen to be smaller than 1 even on the $32\times 32$ lattice. Eventually, for $T\geq 17$, the downward curvature is obvious even on small lattices. Thus, from this plot we read off that $16<T_c<16.5$, leading to the final estimate

$$T_c=16.25\pm 0.25 \tag{80}$$

or

$$\beta_{\rm DG}^c=\frac{T_c}{24}=0.677\pm 0.010\ . \tag{81}$$

Within error bars, this agrees with the value determined by Shugard *et al.*,[21] from measurements of two-dimensional (i.e., unprojected) correlation functions, $\beta_{\rm DG}^c=0.685\pm 0.014$.

In conclusion, our data on $64\times 64$ lattices are in very good agreement with $\beta_{\rm DG}^{R\,c}=\pi/4$. Using this theoretical prediction as input, the "slope criterion" leads to reliable estimates of $T_c$ even on relatively small lattices. In the following analysis of the melting model, we shall therefore use this criterion to identify the transition points.

### 3. *Correlation functions*

Let us start with the low-temperature solid phase, where we expect [recall (58)–(60)]

$$\frac{L}{2}\langle[\bar{h}(x)-\bar{h}(x')]^2\rangle = -4\beta^R\frac{1+\nu}{2}\left[c_4(x-x')+\frac{2l^2}{1+\nu}c_2^{(0)}(x-x')\right], \tag{82}$$

$$\frac{L}{2}\langle[\bar{A}_1(x)-\bar{A}_1(x')]^2\rangle=-4\beta^R c_2^{(1/l)}(x-x')\ , \tag{83}$$

$$\frac{L}{2}\langle[\bar{A}_2(x)-\bar{A}_2(x')]^2\rangle=-4\beta^R\frac{1+\nu}{2}c_2^{(0)}(x-x')\ . \tag{84}$$

Thus, plotting the measured correlation functions on the left-hand side (lhs) versus the theoretical curves on the rhs (see the Appendix), we expect straight lines with slope $4\beta^R(1+\nu)/2$, $4\beta^R$, and $4\beta^R(1+\nu)/2$, respectively. From the aforementioned Coulomb gas argument we know that in the low-temperature phase $\beta^R$ is bounded by $\beta^R\geq\beta_1^R$, where

$$\beta_1^R=\frac{2}{1+\nu}\frac{1}{\pi} \tag{85}$$

is the renormalized inverse temperature at the transition. Hence, with increasing temperature, the slopes $\mathcal{S}$ should decrease until, at the transition, they reach a limiting minimal value which, for $\nu=1$, is in all three cases

$$\mathcal{S}_c=\frac{4}{\pi}=1.2732\ . \tag{86}$$

A typical example for such measurements on $32\times 32$ lattices is shown in Fig. 8 for $l^2=3$ and $T=3$. On the left-hand side, we have plotted the projected correlations versus distance, with crosses (circles) denoting projections onto the $x$ axis ($y$ axis). Although we used at least 250 000 sweeps for equilibration and at least 500 000 sweeps for measurements, the agreement at long distances is not very satisfying. On the right-hand side we have averaged these data and plotted them versus the theoretical curves in (82)–(84). We see that the three correlation functions give consistent estimates for the slope ($\approx 1.33$). Since this is only slightly larger than the critical value (86) we can estimate $T_1\approx 3$. We have analyzed similar runs for various $l^2$ and $T$ (with up to 2 000 000 measurements). As a result we show in Fig. 9 the renormalized temperature, $T^R\equiv 1/\beta^R=4/\mathcal{S}$. We see that $T^R\approx T$, which confirms the above theoretical expectations based on the dilute gas approximation for the defects as discussed after Eq. (51).

Summarizing, we see that over a wide range of $l^2$ the first transition is located around

$$T_1\approx 3\ . \tag{87}$$

The fact that $T_1$ is almost independent of $l$ agrees also with our theoretical expectation on the grounds that physically the transition is caused by the dissociation of dislocation pairs, the *translational* defects of the model. It is intuitively clear that their properties are only weakly dependent on the additional *rotational* energy $\propto l^2$ added in (8), since the potential between dislocations is only modified at short distances $<l$.

For higher temperatures, the fields $A$ become effectively massive and the $h$ correlations are screened at long range to

$$\frac{L}{2}\langle[\bar{h}(x)-\bar{h}(x')]^2\rangle=-4\beta^R l^2 c_2^{(0)}(x-x')\ , \tag{88}$$

which is exactly the behavior in the massless phase of the DG model. At the second transition the renormalized inverse temperature is given by [recall (39)]

$$\beta_2^R=\frac{1}{2\pi l^2}\ . \tag{89}$$

Hence, plotting the $h$ correlations in the intermediate phase versus $-c_2^{(0)}$, we expect again straight lines with a critical slope

$$\mathcal{S}_c=\frac{2}{\pi}=0.6366\ . \tag{90}$$

For $l^2=1.5$, a sequence of such plots for temperatures around the transition point is shown in Fig. 10. Again, the theoretical expectation is very well satisfied. Observe the slight downward curvature for $T>T_2\approx 8.6$ indicating the massive phase. It is, however, much more sensi-

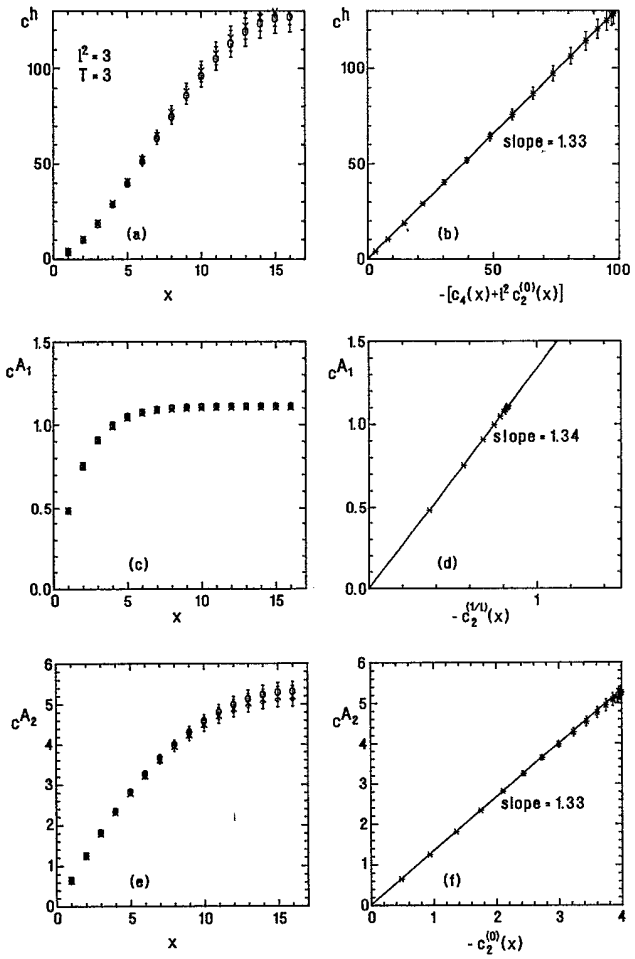


FIG. 8. Projected correlation functions $c^h(x)$ [(a) and (b)], $c^{A_1}(x)$ [(c) and (d)], and $c^{A_2}(x)$ [(e) and (f)] of the melting model for $l^2=3$ and $T=3$ on a $32\times32$ lattice. The data points are averages over 500 000 configurations after discarding at least 250 000 configurations for thermalization. On the lhs we have plotted the projections onto the $x$ axis (○) and $y$ axis (×) separately vs the distance $x$. On the rhs, $x$ and $y$ projections are averaged and plotted vs the theoretically predicted behavior in the massless phase. In such a plot, the data are thus expected to lie on straight lines with slope $4\beta^R\geq 4/\pi=1.273$. This is illustrated by our data for $T=3$, which can clearly be fitted by straight lines with slope $\approx 1.33$. Since this number is only slightly larger than $4/\pi$, we can estimate $T_1\approx 3$.

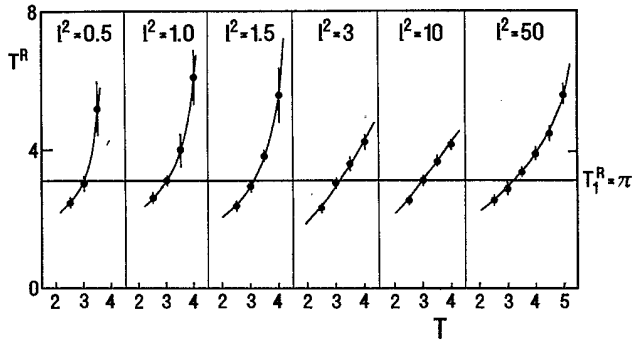


FIG. 9. The renormalized temperature $T^R$ vs $T$ near the low-temperature transition for increasing length scale $l$ of rotational stiffness.

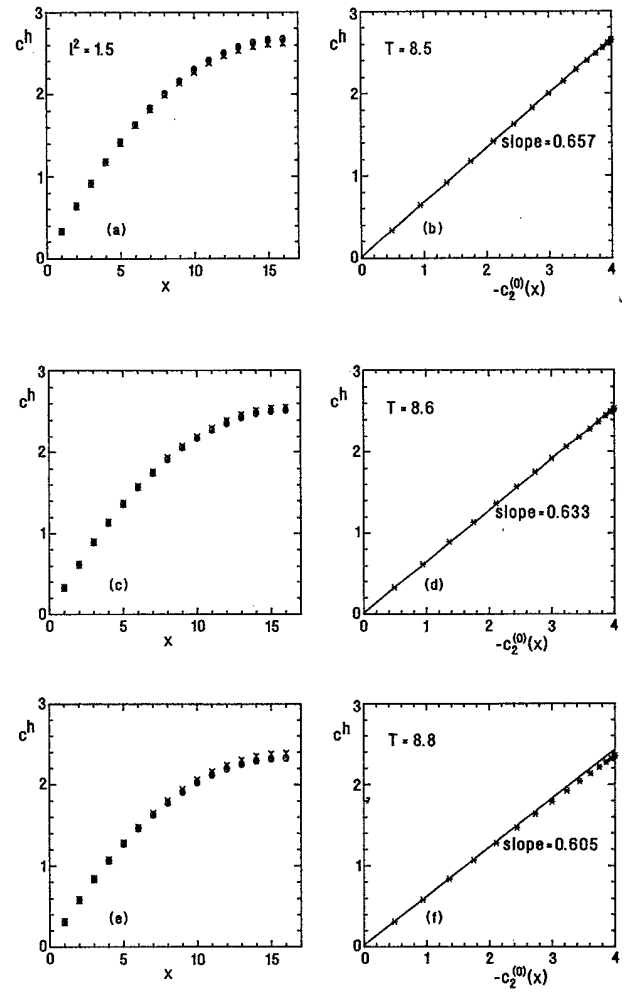


FIG. 10. Projected correlation functions $c^h(x)$ of the melting model near the high-temperature transition for $l^2=1.5$. The lattice size is $32\times32$, and the data are averages over 500 000 configurations. The organization of the plots on the left- and right-hand side is the same as in Fig. 8. Since at the high-temperature transition the critical slope is $2/\pi=0.637$, the data for $T=8.6$ are almost critical. The correlations $c^{A_1}(x)$ and $c^{A_2}(x)$ are not shown since they are massive on both sides of the high-temperature transition.

tive to use the critical slope criterion for locating $T_2$. In this way we estimate $T_2=8.6\pm0.2$ for $l^2=1.5$. Since as a consequence of universality, the results for other values of $l^2$ look very similar we can refrain from showing them here.

## VI. CONCLUSION

The preceding Monte Carlo study confirms that the recently proposed lattice defect model with a rotational stiffness term is sufficiently rich to describe a variety of melting transitions. The distinguishing parameter is the length scale $l$ of rotational stiffness. For very small $l$, there is a single first-order transition which, for increasing $l$, separates into a sequence of two Kosterlitz-Thouless transitions. The model should be relevant for explaining the systematics observed in recent experimental studies of the melting transition in adsorbed layers of long rodlike molecules.[22] In such experiments one also observes the splitting of a single sharp transition into a translational and rotational transition with increasing molecular length, which should be roughly proportional to our model parameter $l$. Certainly, the model will need considerable refinements to cope with realistic materials. As it stands, it is certainly the simplest defect model to illustrate the basic splitting mechanism observed in these materials. It contains no more than the harmonic lattice distortions of translations and rotations plus the associated defects.

## ACKNOWLEDGMENTS

The work was supported in part by Deutsche Forschungsgemeinschaft under Grant No. Kl256.

## APPENDIX: ONE-DIMENSIONAL CORRELATION FUNCTIONS ON A FINITE SQUARE LATTICE

In this Appendix we give analytical expressions for the one-dimensional correlation functions $c_2^{(m)}(x)$ and $c_4(x)$. On a finite square $L\times L$ lattice with spacing $a\equiv1$ and periodic boundary conditions, we find ($k=2\pi n/L$)

$$c_2^{(m)}(x)\equiv\frac{1}{L}\sum_{n=1}^{L-1}\frac{e^{ikx}-1}{2(1-\cos k)+m^2}$$
$$=\frac{1}{2\mathrm{sh}M\,\mathrm{sh}[ML/2]}\left[\mathrm{ch}M\left[x-\frac{L}{2}\right]-\mathrm{ch}M\frac{L}{2}\right]$$
$$=-\frac{\mathrm{sh}[(M/2)x]\mathrm{sh}[(M/2)(L-x)]}{\mathrm{sh}M\,\mathrm{sh}[ML/2]}, \tag{A1}$$

with

$$\mathrm{sh}\frac{M}{2}=\frac{m}{2},\quad \frac{M}{2}=\ln\{m/2+[(m/2)^2+1]^{1/2}\}\ . \tag{A2}$$

$c_2^{(M)}(x)$ is obviously symmetric around $x=L/2$ with

$$c_2^{(m)}\left[\frac{L}{2}\right]=-\frac{1}{2}\frac{\mathrm{th}ML/4}{\mathrm{sh}M}$$

and

$$c_2^{(m)}(0)=c_2^{(m)}(L)=0\ .$$

In the limit $m\to0$, it reduces to

$$c_2^{(0)}(x)=\frac{1}{2L}\left[\left[x-\frac{L}{2}\right]^2-\left[\frac{L}{2}\right]^2\right]$$
$$=-\frac{x}{2}\left[1-\frac{x}{L}\right], \tag{A3}$$

which is a parabola around $x=L/2$, $c_2^{(0)}(L/2)=-L/8$. Note that $c_2^{(0)}(x)/L$ is a universal curve of $\hat{x}=x/L\in[0,1]$, independent of $L$. In order to calculate $c_4(x)$, we consider [$\bar{K}K\equiv2(1-\cos k)$, $k=2\pi n/L$]

$$c_4^{(m)}(x)\equiv\frac{1}{L}\sum_{n=1}^{L-1}\frac{e^{ikx}-1}{\bar{K}K(\bar{K}K+m^2)}$$
$$=\frac{1}{L}\sum_{n=1}^{L-1}\left[\frac{1}{\bar{K}K}-\frac{1}{\bar{K}K+m^2}\right]\frac{1}{m^2}(e^{ikx}-1)$$
$$=\frac{1}{m^2}[c_2^{(0)}(x)-c_2^{(m)}(x)]\ . \tag{A4}$$

Inserting (A1), (A3), and taking the limit $m\to0$, we get

$$c_4^{(0)}(x)\equiv\frac{1}{L}\sum_{n=1}^{L-1}\frac{e^{ikx}-1}{[2(1-\cos k)]^2}$$
$$=\frac{1}{12L}\left\{\left[1+\left[\frac{L}{2}\right]^2\right]\left[\left[x-\frac{L}{2}\right]^2-\left[\frac{L}{2}\right]^2\right]-\frac{1}{2}\left[\left[x-\frac{L}{2}\right]^4-\left[\frac{L}{2}\right]^4\right]\right\}. \tag{A5}$$

Parametrizing $x=L/2-yL/2$ with $y\in[-1,1]$, (A5) can be rewritten as

$$c_4^{(0)}\left[\frac{L}{2}-y\frac{L}{2}\right]=-\frac{L^3}{(16)(12)2}\left\{1+2\left[\frac{2}{L}\right]^2-\left[2+2\left[\frac{2}{L}\right]^2\right]y^2+y^4\right\}. \tag{A6}$$

The polynomial in the curly brackets looks like a double-well potential centered at $y=0$, i.e., $x=L/2$. For large $L$, the point of inflection lies at $y=\sqrt{1/3}=0.5774$ or $x=0.4226(L/2)$, and the curvature at $x=0$ is twice that at $x=L/2$.

[1]D. R. Nelson, Phys. Rev. B **18**, 2318 (1979); D. R. Nelson and B. I. Halperin, *ibid.* **19**, 2457 (1979); A. P. Young, *ibid.* **19**, 1855 (1979).

[2]J. M. Kosterlitz and D. J. Thouless, J. Phys. C **6**, 1181 (1973); Prog. Low Temp. Phys. **7B**, 371 (1978); J. M. Kosterlitz, J. Phys. C **7**, 1946 (1974).

[3]H. Kleinert, Phys. Lett. **91A**, 295 (1982); **95A**, 381 (1983); **96A**, 302 (1983); S. Ami and H. Kleinert, J. Phys. (Paris) Lett. **45**, 877 (1984); H. Kleinert, Phys. Lett. **97A**, 51 (1983).

[4]W. Janke and H. Kleinert, Phys. Lett. **105A**, 1348 (1984); **114A**, 255 (1986). We do not agree with the findings of Ref. 5.

[5]K. J. Strandburg, S. A. Solla, and G. V. Chester, Phys. Rev. B **28**, 2717 (1983); K. J. Strandburg, *ibid.* **34**, 3536 (1986); D. A. Bruce, Mater. Sci. Forum **4**, 51 (1985). For a recent review, see K. J. Strandburg, Rev. Mod. Phys. **60**, 161 (1988); **61**, 747(E) (1989). These authors do not go to large enough lattices to see the characteristic finite-size scaling of the specific-heat peak in a first-order transition as is shown in Ref. 6.

[6]W. Janke and H. Kleinert, Phys. Lett. A **140**, 513 (1989); W. Janke and D. Toussaint, *ibid.* **A116**, 387 (1986).

[7]For a detailed exposition of theoretical and experimental two-dimensional melting see the textbook, H. Kleinert, *Gauge Fields in Condensed Matter* (World Scientific, Singapore, 1989), Vol. II.

[8]M. Bretz, J. G. Dash, D. C. Hickernell, F. O. McLean, and O. E. Vilches, Phys. Rev. A **8**, 1589 (1973); **9**, 2814 (1974) (for $^4$He).

[9]R. Pindak, D. E. Moncton, S. C. Davey, and J. W. Goodby, Phys. Rev. Lett. **46**, 1135 (1981); S. B. Dierker, R. Pindak, and R. B. Meyer, *ibid.* **56**, 1819 (1986); J. D. Brock, A. Aharony, R. J. Birgeneau, K. W. Evans-Lutterodt, J. D. Litster, P. M. Horn, G. B. Stephenson, and A. R. Tajbakhsh, *ibid.* **57**, 98 (1986); A. Aharony, R. J. Birgeneau, J. D. Brock, and J. D. Litster, *ibid.* **57**, 1012 (1986).

[10]H. Kleinert, Phys. Lett. A **130**, 443 (1988).

[11]H. Kleinert, Phys. Lett. A **136**, 468 (1989).

[12]H. Kleinert, Phys. Lett. A **130**, 59 (1988).

[13]W. Janke and H. Kleinert, Phys. Rev. Lett. **61**, 2344 (1988); **62**, 608(E) (1989).

[14]S. T. Chui, Phys. Rev. Lett. **48**, 933 (1982); Phys. Rev. B **28**, 178 (1983).

[15]D. R. Nelson, Phys. Rev. B **26**, 269 (1982).

[16]H. Kleinert, Phys. Lett. A **134**, 217 (1989).

[17]H. Kleinert, Nuovo Cimento Lett. **34**, 464 (1982).

[18]S. Samuel and F.-G. Yee, Nucl. Phys. **B257**, 85 (1985).

[19]J. Tobochnik and G. V. Chester, Phys. Rev. B **20**, 3761 (1979). See also W. J. Shugard, J. D. Weeks, and G. H. Gilmer, *ibid.* **21**, 5309 (1980).

[20]W. Janke and H. Kleinert, Nucl. Phys. **B270**, 135 (1986).

[21]W. J. Shugard, J. D. Weeks, and G. H. Gilmer, Phys. Rev. Lett. **41**, 1399, 1577(E) (1978).

[22]F. Y. Hansen and H. Taub, J. Chem. Phys. **87**, 3232 (1987). For a review see H. Taub, in *The Time Domain in Surface and Structural Dynamics,* Vol. 228 of *NATO Advanced Science Institutes, Series C: Mathematical and Physical Sciences,* edited by G. J. Long and F. Grandjean (Kluwer, Dordrecht, 1988), p. 467. See also H. K. Kim, Q. M. Zhang, and M. H. W. Chan, Phys. Rev. Lett. **56**, 1579 (1986); J. Z. Larese, L. Passell, A. D. Heidemann, D. Richter, and J. P. Wicksted, *ibid.* **61**, 432 (1988); C. Peters, J. A. Morrison, and M. L. Klein, Surf. Sci. **165**, 355 (1986); J. P. Coulomb, M. Bienfait, and J. P. Thorel, Faraday Disc. Chem. Soc. **80**, 79 (1985); J. P. Coulomb and M. Bienfait, J. Phys. (Paris) **47**, 89 (1986); J. W. Osen and S. C. Fain, Jr., Phys. Rev. B **36**, 4074 (1987); H. S. Nham and G. B. Hess, *ibid.* **38**, 5166 (1988); S. Zhang and A. D. Migone, *ibid.* **38**, 12 039 (1988); Surf. Sci. **222**, 31 (1989); J. M. Gay, J. Suzanne, G. Pepe, and T. Meichel, *ibid.* **204**, 69 (1988); R. Wang, H. Taub, H. J. Lauter, J. P. Biberian, and J. Suzanne, J. Chem. Phys. **82**, 3465 (1985); J. C. Newton, Bull. Am. Phys. Soc. **33**, 265 (1988); J. Krim, J. Suzanne, H. Schechter, R. Wang, and H. Taub, Surf. Sci. **162**, 446 (1985); J. R. Dennison, J. C. Newton, S. K. Wang, H. Taub, E. Conrad, J. M. Phillips, and H. Schechter, Bull. Am. Phys. Soc. **33**, 284 (1988).